Check for updates

Synthesis, characterization and synergistic photocatalytic properties of yeast-assisted composite La$_{0.7}$Sr$_{0.3}$MnO$_3$/TiO$_2$

Pan Yue,[a] Zhi-Xian Wei,*[a] Xu-Hong Wu, [b] He-Dan Zhang[a] and Fan Ye[b]

In order to identify a high-efficiency solar-light-driven magnetic photocatalyst, a series of powders such as perovskite La$_{0.7}$Sr$_{0.3}$MnO$_3$, yeast-assisted La$_{0.7}$Sr$_{0.3}$MnO$_3$ (Y-La$_{0.7}$Sr$_{0.3}$MnO$_3$), Y-La$_{0.7}$Sr$_{0.3}$MnO$_3$/TiO$_2$ and TiO$_2$ were prepared and characterized by photoluminescence spectroscopy (PL), UV-Vis diffuse reflectance spectroscopy (DRS), X-ray diffraction (XRD), transmission electron microscopy (TEM), X-ray photoelectron spectroscopy (XPS) and N$_2$ adsorption–desorption (N$_2$-BET). The magnetic and photocatalytic properties of the powders were also investigated. The experimental results show that, when the content of TiO$_2$ in the composite Y-La$_{0.7}$Sr$_{0.3}$MnO$_3$/TiO$_2$ is 3.51 wt%, the Y-La$_{0.7}$Sr$_{0.3}$MnO$_3$/TiO$_2$ exhibits stronger absorption in the UV-Vis light region. A composite p–n heterojunction was formed and had the lowest photoluminescence (PL) intensity, indicating a higher separation efficiency of photogenerated charge carriers and an enhancement of the photocatalytic activity of the Y-La$_{0.7}$Sr$_{0.3}$MnO$_3$/TiO$_2$ composite. Under solar irradiation, Y-La$_{0.7}$Sr$_{0.3}$MnO$_3$/TiO$_2$ shows an obvious synergistic photocatalytic effect on orange (MO) wastewater, and the synergetic index is calculated to be 1.79. Furthermore, it still exhibits high photocatalytic activity after being reused 8 times. Moreover, Y-La$_{0.7}$Sr$_{0.3}$MnO$_3$/TiO$_2$ displays soft ferromagnetic behavior, has much higher magnetization and lower coercivity and remanence. Therefore, Y-La$_{0.7}$Sr$_{0.3}$MnO$_3$/TiO$_2$ can be recycled by an external magnetic field more easily and can be used repeatedly. Radical trapping experiments confirmed that the main reactive oxygen species (ROS) involved in the process of the photocatalytic reaction are the superoxide radical anion ($^{\bullet}$O$_2^-$), hole (h$^+$), and hydroxyl radical ($^{\bullet}$OH), and the sequence of the contributions of the ROS to the photocatalytic activity of the composite is $^{\bullet}$O$_2^-$ > h$^+$ > $^{\bullet}$OH. Furthermore, the photocatalytic mechanism of Y-La$_{0.7}$Sr$_{0.3}$MnO$_3$/TiO$_2$ is proposed in this work.

Introduction

It is well known that multifunctional homogeneous photocatalysts with intrinsic magnetic properties can be recycled *via* a magnetic field. Therefore a lot of homogeneous catalysts with magnetization and photocatalytic properties have been prepared and the corresponding properties investigated recently, for example, rare-earth mixed chalcogenide Dy$_4$S$_4$Te$_3$,[1] multiporous ZnFe$_2$O$_4$ nanotubes,[2] Ni$_2$FeVO$_6$ nanoparticles,[3] (La$_{0.5}$Bi$_{0.2}$Ba$_{0.2}$Mn$_{0.1}$)FeO$_{(3-\delta)}$,[4] porous tetragonal-CuFe$_2$O$_4$ nanotubes,[5] Ba-doped BiFeO$_3$ nanoparticles,[6] ferromagnetic ZrO$_2$ nanostructures,[7] CdS nanostructures,[8] Bi$_5$Fe$_{0.95}$Co$_{0.05}$Ti$_3$-O$_{15}$ *via* europium doping,[9] yttrium ferrite ceramic[10] *etc.* Because of the excellent magnetism and photocatalytic activity of perovskite oxides under solar irradiation, it has become the focus of our research group and some perovskite oxides have

been investigated and reported, such as LaFe$_{0.5}$Mn$_{0.5-x}$O$_{3-\delta}$, LaFe$_{0.9}$Mn$_{0.1-x}$O$_{3-\delta}$, La$_{0.8}$Ba$_{0.2}$Fe$_{0.9}$Mn$_{0.1}$O$_{3-\delta}$ and La$_{0.8}$Sr$_{0.2}$Mn$_{1-x}$-Ti$_x$O$_{3-\delta}$ ($x = 0$–0.15).[11–14]

It is reported that La$_{1-x}$Sr$_x$MnO$_3$ ($x = 0$–0.5) materials show superparamagnetic behaviors and the highest saturation magnetization could be obtained when $x = 0.3$.[15] Furthermore, La$_{1-x}$Sr$_x$MnO$_3$ materials also show good electrical and catalytic properties, so they are always used as multifunctional materials. For example, they have been applied as cathode materials in solid oxide fuel cells,[16–18] and used as catalysts in the degradation of NO[19] and MO.[14] Due to the narrow band gap, La$_{1-x}$Sr$_x$-MnO$_{3-\delta}$ could exhibit good photocatalytic activity under solar light irradiation,[20] and TiO$_2$ displays excellent photocatalytic activities under UV irradiation. So, a composite La$_{0.7}$Sr$_{0.3}$MnO$_3$/TiO$_2$ could improve the utilization of solar energy. Besides, the construction of a heterojunction structure is also a means used in recent years to improve the catalytic activities of pure catalysts. This is because the heterojunction photocatalyst is favorable for the separation of photogenerated electron–hole pairs, so the photocatalytic properties are improved. Therefore, a composite La$_{0.7}$Sr$_{0.3}$MnO$_3$/TiO$_2$ was investigated in this study.

[a]School of Environmental and Safety Engineering, North University of China, Taiyuan, Shanxi, 030051, PR China. E-mail: zx_wei@126.com

[b]Department of Chemistry, Science Institute, North University of China, Taiyuan, Shanxi 030051, P. R. China

Generally speaking, perovskite oxides are usually synthesized at a relatively high calcination temperature, which makes perovskite oxides with very low specific surface areas. To overcome the obstacle of low specific surface areas of perovskite oxides, a lot of approaches have been studied. One of the most effective approaches is to synthesize porous nanostructures, prepared *via* a template method,[21,22] emulsion method,[23,24] spray reaction method,[25] *etc.* Among the template methods, bio-templating has drawn more attention in the field of oxide material synthesis.[26,27] Among many bio-templating agents, yeast can easily be obtained in a large amount in a short time without environmental pollution. Simultaneously, it has a short generation time and can be easily incubated. In addition, yeast as a template may significantly simplify the processing routes because both the synthesis of the template and modification of the template surface can be omitted.[28] So yeast was chosen as a template to increase the specific surface area of $La_{0.7}Sr_{0.3}MnO_3$ and improve its photocatalytic activity.

In a word, in order to identify a high-efficiency solar-light-driven magnetic photocatalyst, a series of powders such as perovskite $La_{0.7}Sr_{0.3}MnO_3$, yeast-assisted $La_{0.7}Sr_{0.3}MnO_3$ (Y-$La_{0.7}Sr_{0.3}MnO_3$), Y-$La_{0.7}Sr_{0.3}MnO_3/TiO_2$ and TiO_2 were prepared and characterized. Simultaneously, the magnetism, the synergistic photocatalytic properties and reusability were also investigated. In addition, we used a range of chemical probes and scavengers for reactive oxygen species (ROS) to interrogate the mechanism of photocatalytic degradation of MO.

Experimental

Materials

The starting chemicals for the target compounds were of analytical grade without further purification. $La(CH_3COO)_3$ (99.9%), $Sr(CH_3COO)_2$ (99%) and $Mn(CH_3COO)_2 \cdot 4H_2O$ (99.9%) *etc.* were purchased from Aladdin Industrial Corporation. Butyl titanate was purchased from Fuchen Chemical Company (Tianjin, China). The powdered yeast was purchased from Angel Yeast Company. The solvents used in this work were purchased from Damao Chemical Company (Tianjin, China). MO was purchased from Tianjin Chemical Reagent Factory.

Preparation of photocatalysts $La_{0.7}Sr_{0.3}MnO_3$, Y-$La_{0.7}Sr_{0.3}MnO_3$, Y-$La_{0.7}Sr_{0.3}MnO_3/TiO_2$ and TiO_2

Preparation of $La_{0.7}Sr_{0.3}MnO_3$. $La_{0.7}Sr_{0.3}MnO_3$ was synthesized according to previous literature.[15] In the typical experiment, the mole ratio of La : Sr : Mn was 0.7 : 0.3 : 1, and metal acetate salts were dissolved in deionized water; the mixed solution was named A. A was thermally decomposed in an oven under normal atmosphere at 800 °C for 1.5 h and left to cool down to room temperature before being ground to obtain $La_{0.7}Sr_{0.3}MnO_3$.

Preparation of Y-$La_{0.7}Sr_{0.3}MnO_3$. Y-$La_{0.7}Sr_{0.3}MnO_3$ was synthesized using yeast-assisted thermal-hydro decomposition. In this experiment, the solution A was prepared and poured into the activated yeast solution (0.5000 g powdered yeast cultivated in 20.0 ml 37 °C water for 0.5 h). The mixed solution was stirred

with a magnetic stirrer at 37 °C for an hour, and then decomposed in an oven at 800 °C for 1.5 h. The obtained powder was ground to obtain Y-$La_{0.7}Sr_{0.3}MnO_3$.

Preparation of TiO_2. TiO_2 was synthesized using a sol–gel method.[29] 10.0 ml butyl titanate was added to a mixed solvent of 70.0 ml absolute ethanol, 10.0 ml H_2O and 4.0 ml acetic acid, which was on a magnetic stirrer to obtain a uniform sol. Then, the mixture was dried in an oven at 80 °C and calcined in a muffle furnace at 550 °C for 1.5 h and left to cool down to room temperature before being ground to obtain a TiO_2 powder.

Preparation of Y-$La_{0.7}Sr_{0.3}MnO_3/TiO_2$. Y-$La_{0.7}Sr_{0.3}MnO_3/TiO_2$ was prepared using a sol–gel method. Firstly, two mixed solutions were prepared. 0.2000 g Y-$La_{0.7}Sr_{0.3}MnO_3$ powder was dispersed in a mixed solvent of 35.0 ml absolute ethanol, 10.0 ml H_2O and 4.0 ml acetic acid, which was named B. Different amounts of butyl titanate were added to 35.0 ml absolute ethanol, which was on a magnetic stirrer to obtain a uniform sol (named C). Then, C was slowly dropwise added to B under vigorous mechanical stirring in a 40 °C water bath for 2 h. Then, the mixture was dried in an oven at 80 °C and calcined in a muffle furnace at 550 °C for 1.5 h and left to cool down to room temperature before being ground to obtain Y-$La_{0.7}Sr_{0.3}MnO_3/TiO_2$ powders. The mass fraction of TiO_2 on Y-$La_{0.7}Sr_{0.3}MnO_3$ was determined from the titanium dioxide converted from the butyl titanate and the composite substance was recorded as Y-$La_{0.7}Sr_{0.3}MnO_3/TiO_2$ (χ wt%) (χ = 0.47, 1.17, 3.51 and 5.86).

Characterization

X-ray diffraction (XRD) was used to identify the phase and crystalline nature of the samples, and was performed on a D/max-RB X-ray diffraction apparatus (Rigaku) with a Ni-filtered CuKα radiation source (λ = 1.5418 Å). UV-Vis DRS was conducted using a UV-Vis spectrophotometer (Hitachi, Japan), using $BaSO_4$ as a reflectance sample, and the mass of all of the as-prepared samples was equal to 0.0020 g. The measurement of PL spectra was performed on a fluorescence spectrophotometer (F-2700, Hitachi) with a Xe lamp as the excitation source (a perovskite catalyst with a wavelength of 220 nm was used; under this wavelength the emission band of TiO_2 was covered by a frequency-doubled peak, so the excitation wavelength of TiO_2 was 265 nm). N_2-physisorption analysis of the prepared catalysts was performed at 200 °C on a NOVA touch-LX^4 surface area & pore size analyzer to obtain the textural properties of the catalysts (specific surface area and pore volume). The particle size and morphology of the samples were characterized by a JEM-2100 (200 kV) transmission electron microscope (TEM). The selected area electron diffraction (SAED) patterns from the TEM and high resolution TEM (HRTEM) images were analyzed. XPS analysis was performed by a PHI Quantera SXM apparatus, equipped with a standard Al Kα excitation source. The binding energy (BE) scale has been calibrated by measuring the C 1s peak (BE = 284.6 eV) from the ubiquitous surface layer of adventitious carbon. The magnetic measurements of the samples were carried out in a vibrating sample magnetometer

(VSM) (VersaLad, Quantum Design Co., America) at room temperature in an applied magnetic field sweeping between ±30 000 Oe. An image of the yeast cells was recorded with a polarizing microscope (TL-1530, Shanghai Di Lun Optical Instrument Co., Ltd.)

Photocatalytic experiments. Photocatalytic experiments were conducted out of the chemistry department building between 9:30 a.m. and 3:30 p.m. on a sunny day, July 2016. In that period, the solar intensity fluctuation was minimal and the intensity was about 97 100 lux in the city of Taiyuan ($112°33'00''$-E, $37°51'9''$-N). The photocatalytic activity of the as-prepared catalysts was evaluated using MO as a probe subject. In this experiment, 0.0050 g $Y-La_{0.7}Sr_{0.3}MnO_3$, $Y-La_{0.7}Sr_{0.3}MnO_3/TiO_2$ and TiO_2 were dispersed into 50.0 ml MO solution (10 mg l^{-1}, pH = 3.0) in a glass reactor, which was put in the dark for 10 min to achieve adsorption–desorption equilibrium between MO and the photocatalyst. After that, the reactor was irradiated with sunlight under mechanical stirring. After the photo-catalysis experiment, the powder was recovered from the solution with a magnet (50 mm × 50 mm × 10 mm, surface field of ∼3000 G), and the concentration of the MO solution was determined using the UV-Vis spectrophotometer according to its absorbance wavelength at 505 nm. 4.0 ml MO solutions were taken at regular 5 min intervals during the irradiation, and were analyzed using the UV-Vis spectrometer. The MO degradation percentage was calculated as:

$$\text{Degradation rate (\%)} = 100(C_0 - C_t)/C_0 \qquad (1)$$

where C_0 and C_t (mg L^{-1}) are the concentrations of the MO solution before and after the photocatalytic degradation, respectively.

Scavenger studies. Sacrificial substrates that have high affinities for particular ROS have been reported as a method to differentiate the contribution of each ROS to the photocatalytic activity of novel materials. In this study, isopropanol (IPA, 0.1 mM), p-benzoquinone (BQ, 0.1 mM), and potassium iodide (KI, 0.1 mM) were adopted to be scavengers of the hydroxyl radicals ($^•OH$), superoxide radicals ($^•O_2^-$) and holes (h^+), respectively,[30,31] and the experiment was carried out according to the steps of "Photocatalytic experiments" described above.

Results and discussion

XRD analysis

The XRD patterns of the as-prepared $La_{0.7}Sr_{0.3}MnO_3$, $Y-La_{0.7}Sr_{0.3}MnO_3$ and $Y-La_{0.7}Sr_{0.3}MnO_3/TiO_2$ (3.51 wt%) are shown in Fig. 1. The samples exhibit a clear rhombohedral structure with characteristic 2θ values at $32.7°$, $40.1°$, $46.8°$, $58.1°$ and $68.5°$ (JCPDS no. 89-0649). No other peak is found, indicating that the perovskite oxides $La_{0.7}Sr_{0.3}MnO_3$, $Y-La_{0.7}Sr_{0.3}MnO_3$ and $Y-La_{0.7}Sr_{0.3}MnO_3/TiO_2$ were formed. In addition, it is noted that all of the recorded diffraction spectra reveal only the diffraction peaks of perovskite oxide $La_{0.7}Sr_{0.3}MnO_3$, without any additional diffraction peaks relating to Ti, which could be attributed to the low content of TiO_2 (ref. 32) that did not result in any significant change in the crystalline phase of $Y-La_{0.7}Sr_{0.3}MnO_3/$

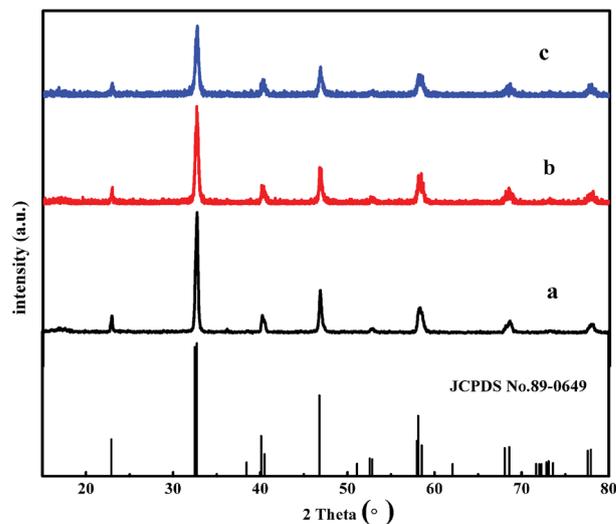Fig. 1 XRD patterns of (a) $La_{0.7}Sr_{0.3}MnO_3$, (b) $Y-La_{0.7}Sr_{0.3}MnO_3$, and (c) $Y-La_{0.7}Sr_{0.3}MnO_3/TiO_2$ (3.51 wt%).

TiO_2. As shown in Fig. 1, the diffraction peak positions of $La_{0.7}Sr_{0.3}MnO_3$, $Y-La_{0.7}Sr_{0.3}MnO_3$ and $Y-La_{0.7}Sr_{0.3}MnO_3/TiO_2$ do not change, but the intensities of the characteristic diffraction peaks of $Y-La_{0.7}Sr_{0.3}MnO_3$ and $Y-La_{0.7}Sr_{0.3}MnO_3/TiO_2$ are weaker than those of $La_{0.7}Sr_{0.3}MnO_3$. Additionally, the peaks of $La_{0.7}Sr_{0.3}MnO_3$, $Y-La_{0.7}Sr_{0.3}MnO_3$ and $Y-La_{0.7}Sr_{0.3}MnO_3/TiO_2$ (3.51 wt%) become wider and wider in sequence, indicating that the crystallite sizes decrease in sequence according to Debye–Scherrer's formula, which is consistent with the results of the TEM. Those results indicate that the crystallite volumes indeed decrease with the addition of yeast, and that may result in bigger surface areas and higher photocatalytic activity of the as-prepared powders.

PL analysis

Photoluminescence (PL) is a powerful technique to investigate the separation efficiency of photogenerated electrons and holes of photocatalysts. PL emission results from the recombination of photogenerated electrons and holes and the PL intensity indicates the recombination rate of electron–hole pairs under light irradiation.[33,34] In Fig. 2(a), the peaks at 405–500 nm are
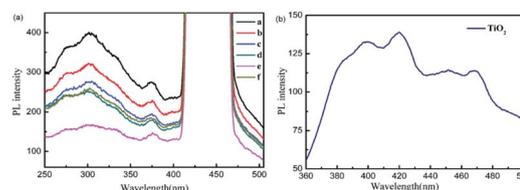

Fig. 2 (a) Photoluminescence spectra of the catalysts (with an excitation wavelength of 220 nm): (a) $La_{0.7}Sr_{0.3}MnO_3$, (b) $Y-La_{0.7}Sr_{0.3}MnO_3$, (c) $Y-La_{0.7}Sr_{0.3}MnO_3/TiO_2$ (0.47 wt%), (d) $Y-La_{0.7}Sr_{0.3}MnO_3/TiO_2$ (1.17 wt%), (e) $Y-La_{0.7}Sr_{0.3}MnO_3/TiO_2$ (3.51 wt%) and (f) $Y-La_{0.7}Sr_{0.3}MnO_3/TiO_2$ (5.86 wt%). (b) Photoluminescence spectra of TiO_2 (with an excitation wavelength of 265 nm).

frequency-doubled peaks of the prepared powders (a–f). The PL spectra of Y-La$_{0.7}$Sr$_{0.3}$MnO$_3$/TiO$_2$, Y-La$_{0.7}$Sr$_{0.3}$MnO$_3$ and La$_{0.7}$Sr$_{0.3}$MnO$_3$ exhibit a wide and strong emission band which is observed between 250 and 405 nm. Here, it is worth noting that the PL spectrum of TiO$_2$ is shown in Fig. 2(b) (where the excitation wavelength was 265 nm), and the emission band is between 360 and 500 nm. However, with an excitation wavelength of 220 nm, the emission band of TiO$_2$ was covered by a frequency-doubled peak, so the PL intensity of TiO$_2$ cannot be compared with the perovskite oxide Y-La$_{0.7}$Sr$_{0.3}$MnO$_3$/TiO$_2$. Therefore, the PL intensity of Y-La$_{0.7}$Sr$_{0.3}$MnO$_3$/TiO$_2$ was compared with that of Y-La$_{0.7}$Sr$_{0.3}$MnO$_3$ to investigate the recombination rate of electron–hole pairs of the composites. As can be seen from Fig. 2(a), although the PL curve of Y-La$_{0.7}$Sr$_{0.3}$MnO$_3$ is similar to that of La$_{0.7}$Sr$_{0.3}$MnO$_3$, the PL intensity of Y-La$_{0.7}$Sr$_{0.3}$MnO$_3$ is obviously weaker than that of La$_{0.7}$Sr$_{0.3}$MnO$_3$, indicating that the recombination rate of electron–hole pairs is decreased and the catalytic activity of Y-La$_{0.7}$Sr$_{0.3}$MnO$_3$ could be higher than that of La$_{0.7}$Sr$_{0.3}$MnO$_3$. So Y-La$_{0.7}$Sr$_{0.3}$MnO$_3$ was chosen to synthesize the composite Y-La$_{0.7}$Sr$_{0.3}$MnO$_3$/TiO$_2$ in this study. As shown in Fig. 2(a), the PL intensity decreases with increasing content of TiO$_2$ from 0 to 3.51 wt%, and the PL intensity increases when the TiO$_2$ content is up to 5.86 wt%. This result means that when the content of the TiO$_2$ in Y-La$_{0.7}$Sr$_{0.3}$MnO$_3$/TiO$_2$ is 3.51 wt%, the composite Y-La$_{0.7}$Sr$_{0.3}$MnO$_3$/TiO$_2$ (3.51 wt%) has the lowest PL intensity, indicating that a Y-La$_{0.7}$Sr$_{0.3}$MnO$_3$/TiO$_2$ heterojunction can effectively suppress the recombination of electron–hole pairs and Y-La$_{0.7}$Sr$_{0.3}$MnO$_3$/TiO$_2$ (3.51 wt%) could be the best photocatalyst among the prepared powders.

UV-Vis Diffuse Reflection Spectroscopy (DRS) analysis

The photoabsorption properties of the as-prepared TiO$_2$, La$_{0.7}$Sr$_{0.3}$MnO$_3$, Y-La$_{0.7}$Sr$_{0.3}$MnO$_3$ and the composite Y-La$_{0.7}$Sr$_{0.3}$MnO$_3$/TiO$_2$ (3.51 wt%) (the four samples had the same mass in the UV-Vis DRS test) were detected by UV-Vis DRS, as shown in Fig. 3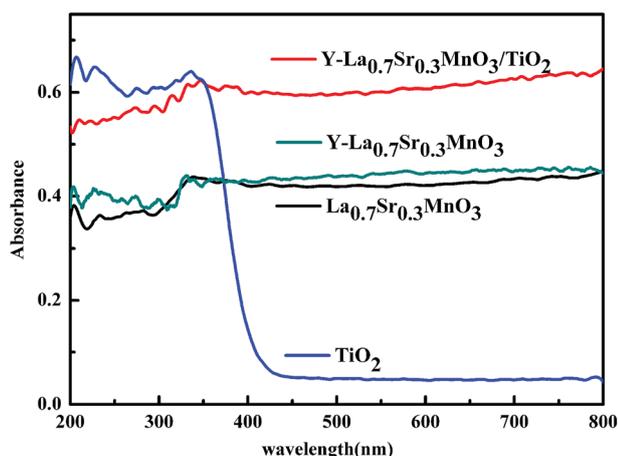. It can be observed that only UV light is absorbed by the TiO$_2$, which is ascribed to electron excitations of TiO$_2$ from the valence band to the conduction band. While La$_{0.7}$Sr$_{0.3}$MnO$_3$, Y-La$_{0.7}$Sr$_{0.3}$MnO$_3$ and Y-La$_{0.7}$Sr$_{0.3}$MnO$_3$/TiO$_2$ (3.51 wt%) all exhibit broad absorption from UV to visible light, and the absorbance increases in sequence, which indicates that Y-La$_{0.7}$Sr$_{0.3}$MnO$_3$/TiO$_2$ (3.51 wt%), with higher absorbance, could have higher photocatalytic activities, and would be a high-efficiency solar-light-driven photocatalyst.

XPS analysis

To verify if titanium exists in Y-La$_{0.7}$Sr$_{0.3}$MnO$_3$/TiO$_2$ (3.51 wt%), an XPS experiment was performed and the results are shown in Fig. 4. Fig. 4(a) shows that La, Sr, Mn, Ti, O and C are detected on the surface of the sample. Fig. 4(b) shows the XPS spectrum of the Ti 2p region. It demonstrates that two peaks for Ti 2p$_{3/2}$ and Ti 2p$_{1/2}$ are located at 457.8 eV and 463.6 eV, respectively.[35] The spin orbit splitting energy between Ti 2p$_{3/2}$ and Ti 2p$_{1/2}$ is 5.8 eV and in agreement with the result of Ti 2p corresponding to Ti^{4+} and only consisting of the Ti^{4+} chemical state.[36] Thus the existence of titanium in Y-La$_{0.7}$Sr$_{0.3}$MnO$_3$/TiO$_2$ (3.51 wt%) is verified, and is in the form of TiO$_2$.

The XPS spectra of Mn 2p$_{1/2}$ and Mn 2p$_{3/2}$ of Y-La$_{0.7}$Sr$_{0.3}$MnO$_3$/TiO$_2$ (3.51 wt%) are shown in Fig. 4(c). The full width at half maximum (FWHM) of the Mn 2p$_{3/2}$ peak for the sample is larger than 6 eV, which explicitly indicates the coexistence of Mn^{2+}, Mn^{3+} and Mn^{4+} ions.[37] It is reported that the binding energy (BE) values of Mn 2p$_{3/2}$ and Mn 2p$_{1/2}$ for the manganese cations in Mn^{2+}, Mn^{3+} and Mn^{4+} are 641.0, 641.9, 642.1, 652.7, 653.1, and 653.8 eV, respectively.[37–39] While in this study, the peaks of Mn 2p$_{3/2}$ and Mn 2p$_{1/2}$ for the manganese cations in Mn^{2+}, Mn^{3+} and Mn^{4+} are 641.3, 642.3, 644.55, 652.55, 653.7, and 655.5 eV, respectively. It is obviously shown that the Mn 2p$_{3/2}$ and Mn 2p$_{1/2}$ shift to higher BEs, which have been found in previous literature.[37] Meanwhile, the multivalent state of Mn can result in a higher catalytic oxidation activity. So Y-La$_{0.7}$Sr$_{0.3}$MnO$_3$/TiO$_2$ (3.51 wt%) could be used as a high efficiency photocatalyst.
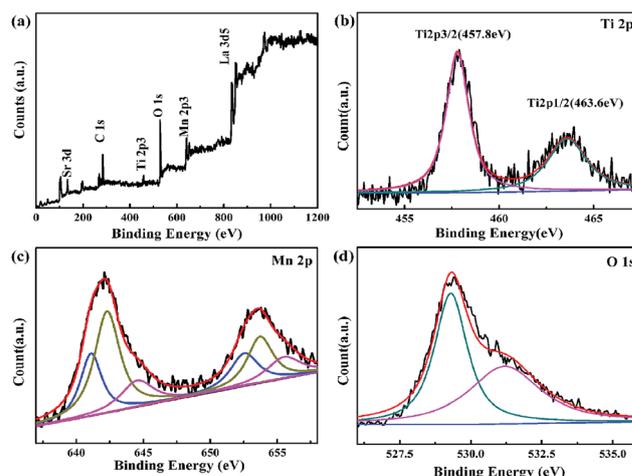

Fig. 3 UV-Vis diffuse reflectance spectra of TiO$_2$, La$_{0.7}$Sr$_{0.3}$MnO$_3$, Y-La$_{0.7}$Sr$_{0.3}$MnO$_3$, and Y-La$_{0.7}$Sr$_{0.3}$MnO$_3$/TiO$_2$ (3.51 wt%).

Fig. 4 XPS spectra of Y-La$_{0.7}$Sr$_{0.3}$MnO$_3$/TiO$_2$ (3.51 wt%) sample, (a) survey scan, (b) Ti 2p, (c) Mn 2p, (d) O 1s.

In Fig. 4(d), O 1s is decomposed into two peaks at binding energies of 529.3 eV and 531.2 eV,[40] where the two peaks stand for the lattice oxygen (O_{latt}) and surface-adsorbed oxygen (O_{ads}), respectively. O_{ads} is the important component for improving photocatalytic properties.

TEM analysis

TEM images of $La_{0.7}Sr_{0.3}MnO_3$, Y-$La_{0.7}Sr_{0.3}MnO_3$ and Y-$La_{0.7}$-$Sr_{0.3}MnO_3/TiO_2$ (3.51 wt%) are displayed in Fig. 5(a–c), and a high resolution TEM (HRTEM) image of Y-$La_{0.7}Sr_{0.3}MnO_3/$ TiO_2 (3.51 wt%) with the corresponding SAED pattern is shown in Fig. 5(d). It is evident from the TEM images of the samples in Fig. 5(a–c) that the particle sizes of the catalysts are about 40–150 nm, with the average particle sizes of $La_{0.7}Sr_{0.3}MnO_3$, Y-$La_{0.7}Sr_{0.3}MnO_3$ and Y-$La_{0.7}Sr_{0.3}MnO_3/TiO_2$ (3.51 wt%) being about 132 nm, 63 nm and 43 nm (measured by nano measurer software), respectively. The results indicate that the addition of yeast reduces the particle volume of the samples (corresponding to the results of the XRD) and could enhance their photocatalytic activity. From Fig. 5(d), by measuring the lattice fringes, the resolved interplanar distances are determined to be around 2.82 and 3.89 Å, corresponding to the (102) plane of TiO_2 (JCPDS no. 65-6429) and the (012) plane of Y-$La_{0.7}Sr_{0.3}$-MnO_3, respectively. As Y-$La_{0.7}Sr_{0.3}MnO_3$ is a p-type semiconductor[41] and TiO_2 is an n-type semiconductor,[42] the results above further demonstrate that composite Y-$La_{0.7}Sr_{0.3}MnO_3/$ TiO_2 is successfully synthesized and a p–n heterojunction is formed. Here, the heterojunction interface formed in the Y-$La_{0.7}Sr_{0.3}MnO_3/TiO_2$ may help to effectively separate electron–hole pairs by shortening the charge transfer distance.[43] This is in agreement with the PL results, indicating that the composite Y-$La_{0.7}Sr_{0.3}MnO_3/TiO_2$ could enhance the photocatalytic activity.

BET analysis

The results of the adsorption–desorption isotherms indicate that TiO_2, $La_{0.7}Sr_{0.3}MnO_3$, Y-$La_{0.7}Sr_{0.3}MnO_3$ and Y-$La_{0.7}Sr_{0.3}MnO_3/TiO_2$ (3.51 wt%) have type III isotherm shapes, which exhibit type H3 hysteresis loops as can be seen in Fig. 6(a).[44] The adsorption and desorption lines overlaps completely in the low relative pressure range, which is mainly due to a presence of non-pores. Even though the samples in this study belong to the type III-class, there are hysteresis loops in the high relative pressure region ($P/P_0 > 0.8$), which are proposed to be a result of bulk pores due to agglomeration of particles.

As shown in Table 1, the addition of yeast in the synthesis process of Y-$La_{0.7}Sr_{0.3}MnO_3$ leads to an increase in the BET surface area. This can be attributed to the effect of the yeast template. An optical image of yeast cells shows that the shape of the yeast cells is spherical Fig. 6(b). During the preparation of Y-$La_{0.7}Sr_{0.3}MnO_3$, hybrid precursors formed on the yeast cell walls were scattered evenly by the yeast template. When the hybrid precursors were calcined, the aggregation of the precursor was inhibited by the scattered spherical yeast cells. Hence, compared with $La_{0.7}Sr_{0.3}MnO_3$ which was not added to yeast in the synthetic process, the BET surface area of Y-$La_{0.7}Sr_{0.3}MnO_3$ increases.

Magnetic properties

The room temperature magnetic hysteresis curves obtained from VSM measurements are shown in Fig. 7(a), and the magnetic parameters such as the saturation magnetization M_s, (M_s measured at 28.6 kOe), coercivity H_c and remanent magnetization M_r are given in Table 2. It is seen that the powders show no obvious magnetic hysteresis loops and low coercivities H_c and remanences M_r, and exhibit soft ferromagnetic behavior. The M_s value for Y-$La_{0.7}Sr_{0.3}MnO_3$ is similar to the value for $La_{0.7}Sr_{0.3}MnO_3$, but the corresponding value for Y-$La_{0.7}Sr_{0.3}MnO_3/TiO_2$ (3.51 wt%) is lower than those of both of them. The decrease in the value for Y-$La_{0.7}Sr_{0.3}MnO_3/TiO_2$ (3.51 wt%) is attributed to magnetization shielding provided by the non-magnetic TiO_2. It is noted that in spite of the decrease in the M_s of Y-$La_{0.7}Sr_{0.3}MnO_3/TiO_2$ (3.51 wt%), the value is still large enough to achieve simple separation with an external magnetic field (50 mm × 50 mm × 10 mm, surface field of $\sim$3000 G) (Fig. 7(b)). As shown in the above experimental data, the composite Y-$La_{0.7}Sr_{0.3}MnO_3/TiO_2$ (3.51 wt%) exhibits stronger absorption in the UV-Vis light region, higher separation efficiency of photogenerated charge carriers and higher
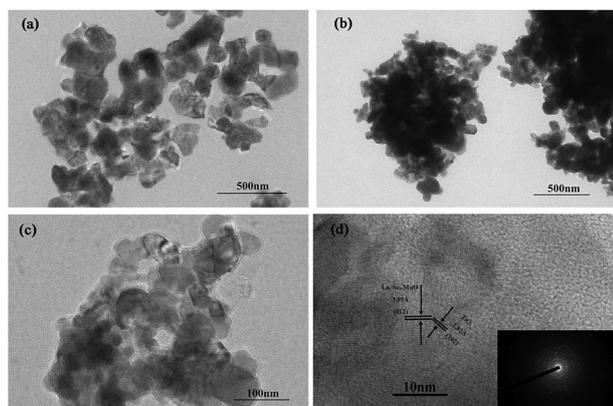

Fig. 5 TEM images of (a) $La_{0.7}Sr_{0.3}MnO_3$, (b) Y-$La_{0.7}Sr_{0.3}MnO_3$, (c) Y-$La_{0.7}Sr_{0.3}MnO_3/TiO_2$ (3.51 wt%) and (d) lattice fringes from HRTEM image with corresponding SAED pattern of Y-$La_{0.7}Sr_{0.3}MnO_3/TiO_2$ (3.51 wt%).
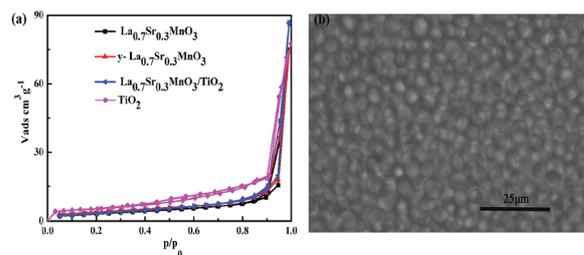

Fig. 6 (a) Adsorption–desorption isotherms of N_2 for TiO_2, $La_{0.7}$-$Sr_{0.3}MnO_3$, Y-$La_{0.7}Sr_{0.3}MnO_3$ and Y-$La_{0.7}Sr_{0.3}MnO_3/TiO_2$ (3.51 wt%). (b) Optical image of yeast cells.

Table 1 Overview of the surface properties of as-prepared samples

Sample	S_{BET} (m^2 g^{-1})	Pore radius $D_v(r)$ (nm)
TiO$_2$	1.85	8.67
La$_{0.7}$Sr$_{0.3}$MnO$_3$	11.86	16.64
Y-La$_{0.7}$Sr$_{0.3}$MnO$_3$	14.02	15.46
Y-La$_{0.7}$Sr$_{0.3}$MnO$_3$/TiO$_2$	12.77	16.41
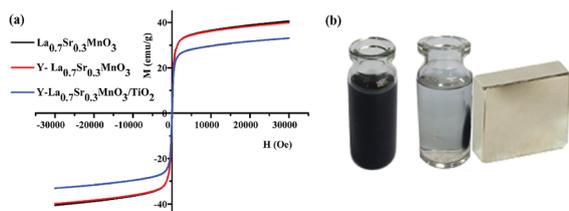
Fig. 7 (a) M−H hysteresis loops of La$_{0.7}$Sr$_{0.3}$MnO$_3$, Y-La$_{0.7}$Sr$_{0.3}$MnO$_3$ and Y-La$_{0.7}$Sr$_{0.3}$MnO$_3$/TiO$_2$ at room temperature. (b) Magnetic composite Y-La$_{0.7}$Sr$_{0.3}$MnO$_3$/TiO$_2$ (3.51 wt%) was absolutely recovered from the solution by a magnet.

Table 2 Magnetic data for La$_{0.7}$Sr$_{0.3}$MnO$_3$, Y-La$_{0.7}$Sr$_{0.3}$MnO$_3$ and Y-La$_{0.7}$Sr$_{0.3}$MnO$_3$/TiO$_2$ (3.51 wt%)

Sample	H_c (Oe)	M_r (emu g^{-1})	M_s (emu g^{-1})
La$_{0.7}$Sr$_{0.3}$MnO$_3$	41.4	2.0	40.1
Y-La$_{0.7}$Sr$_{0.3}$MnO$_3$	38.3	1.9	39.4
Y-La$_{0.7}$Sr$_{0.3}$MnO$_3$/TiO$_2$	24.8	0.7	32.6

saturation magnetization, therefore, this study continuously investigates its photocatalytic activities under sunlight.

Synergetic photocatalytic effect of Y-La$_{0.7}$Sr$_{0.3}$MnO$_3$/TiO$_2$ (3.51 wt%)

Before the photocatalysis, the adsorption performance of the photocatalysts was investigated. As shown in Fig. 8(a), in the dark the adsorption capacities of TiO$_2$, Y-La$_{0.7}$Sr$_{0.3}$MnO$_3$ and Y-La$_{0.7}$Sr$_{0.3}$MnO$_3$/TiO$_2$ (3.51 wt%) become stronger and stronger in sequence. Here, the adsorption capacities could be attributed to the specific surface areas and pore radii which could promote the adsorption capacity of the organic pollutants. In this study, the BET surface area and pore radius of TiO$_2$ are smaller than those of Y-La$_{0.7}$Sr$_{0.3}$MnO$_3$ and Y-La$_{0.7}$Sr$_{0.3}$MnO$_3$/TiO$_2$ (see Table 1), and hence it has the lowest adsorption capacity among the examined powders. The pore radius of Y-La$_{0.7}$Sr$_{0.3}$MnO$_3$/TiO$_2$ is bigger than that of Y-La$_{0.7}$Sr$_{0.3}$MnO$_3$ while the specific surface area of the composite is smaller. The higher adsorption capacity of the composite shows that the pore radius is the deciding factor for the adsorption of large MO molecules.

After adsorption, the photocatalytic activities of the as-prepared samples were evaluated by exposing them to the irradiation of solar light. For a blank experiment without catalysts, MO degradation under sunlight illumination is negligible (data not shown). As shown in Fig. 8(a), one can observe that Y-
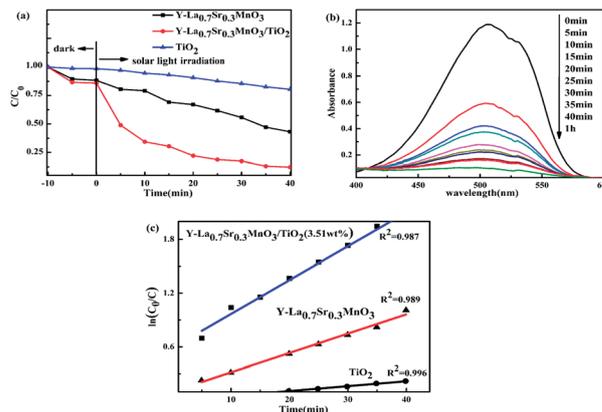

Fig. 8 (a) Evolution of MO concentration according to sunlight radiation exposure time in the presence of different catalysts. (b) The UV-Vis spectral changes of MO degraded by Y-La$_{0.7}$Sr$_{0.3}$MnO$_3$/TiO$_2$ (3.51 wt%). (c) First order kinetics curves of the degradation of MO with different catalysts.

La$_{0.7}$Sr$_{0.3}$MnO$_3$/TiO$_2$ (3.51 wt%) possesses remarkably improved photocatalytic activity over Y-La$_{0.7}$Sr$_{0.3}$MnO$_3$ and TiO$_2$, and exhibits the best degradation efficiency with about 90% MO removal after 40 min of sunlight irradiation. In Fig. 8(b), it shows the change of absorbance with time. In addition, the degradation of MO approximately followed first order kinetics, as evidenced by the linear plot of $-\ln(C/C_0)$ vs. photocatalytic time t (Fig. 8(c)). We obtained the rate constants of k_1 (Y-La$_{0.7}$Sr$_{0.3}$MnO$_3$/TiO$_2$), k_2 (Y-La$_{0.7}$Sr$_{0.3}$MnO$_3$) and k_3 (TiO$_2$) to be 3.67 $\times 10^{-2}$ min^{-1}, 2.103 $\times 10^{-2}$ min^{-1} and 0.546 $\times 10^{-2}$ min^{-1}, respectively. Furthermore, the MO degradation rate constant of Y-La$_{0.7}$Sr$_{0.3}$MnO$_3$/TiO$_2$ was found to be even higher than the sum of Y-La$_{0.7}$Sr$_{0.3}$MnO$_3$ and TiO$_2$, which suggests that the synergetic effect of Y-La$_{0.7}$Sr$_{0.3}$MnO$_3$/TiO$_2$ could contribute to the whole catalytic activity. Here, we quantitatively evaluate the synergetic effect in the MO degradation system by using the SI:[45]

$$SI = k_1/[(1 - x)k_2 + xk_3] \qquad (2)$$

where x is the content of TiO$_2$ in Y-La$_{0.7}$Sr$_{0.3}$MnO$_3$/TiO$_2$ (3.51 wt%); here $x = 3.51\%$. k_1, k_2 and k_3 are the first-order rate constants of Y-La$_{0.7}$Sr$_{0.3}$MnO$_3$/TiO$_2$ (3.51 wt%), Y-La$_{0.7}$Sr$_{0.3}$MnO$_3$ and TiO$_2$, respectively. The value of SI was obtained to be 1.79, implying that this synergistic effect can enhance the catalytic activity of Y-La$_{0.7}$Sr$_{0.3}$MnO$_3$/TiO$_2$ (3.51 wt%) by 79.0%.

The photocatalytic recyclability and repeated performance of Y-La$_{0.7}$Sr$_{0.3}$MnO$_3$/TiO$_2$ (3.51 wt%) were studied using the photocatalytic degradation of MO under sunlight irradiation for 50 min. After each cycling photocatalytic experiment, the photocatalyst was collected using a magnet for the next recycling. From Fig. 9, the photocatalytic degradation efficiency slightly dropped over 8 cycles, however, the photocatalyst Y-La$_{0.7}$Sr$_{0.3}$MnO$_3$/TiO$_2$ (3.51 wt%) still maintained high photocatalytic activity, indicating that Y-La$_{0.7}$Sr$_{0.3}$MnO$_3$/TiO$_2$ is very stable under the photocatalytic reaction conditions, and it can be recycled by magnetic field and possesses high reusability.
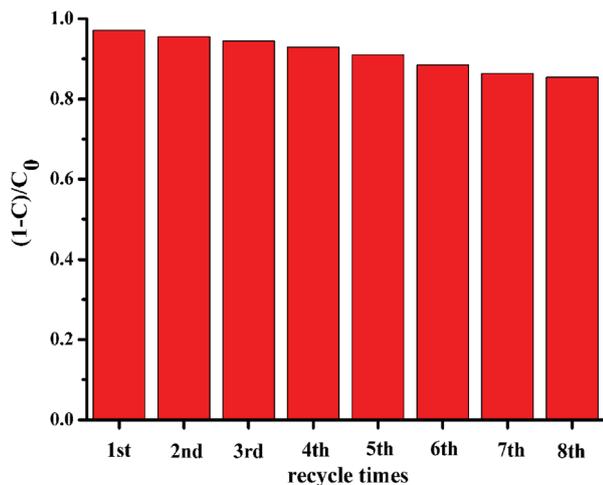
Fig. 9 The recycled photocatalytic experiments of Y-La$_{0.7}$Sr$_{0.3}$MnO$_3$/TiO$_2$ (3.51 wt%) for the degradation of MO under sunlight.

Photocatalytic mechanism

Active species trapping experiments. In the photocatalytic degradation process, a series of photogenerated main active species of h$^+$, $\cdot$OH and $\cdot$O$_2^-$ are suspected to be involved in the photocatalytic reaction. To further evaluate the roles of these active species during the photodegradation of MO, different scavengers were introduced to quench the relevant active species. As shown in Fig. 10, the photocatalytic degradation of MO over the Y-La$_{0.7}$Sr$_{0.3}$MnO$_3$/TiO$_2$ composite was affected by the addition of different scavengers, and the sequence of the photocatalytic degradation efficiency of MO in descending order is isopropanol (IPA: the scavenger of $\cdot$OH) > potassium iodide (KI: the scavenger of h$^+$) > p-benzoquinone (BQ: the scavenger of $\cdot$O$_2^-$), indicating that superoxide radicals ($\cdot$O$_2^-$), holes (h$^+$) and hydroxyl radicals ($\cdot$OH) are all active species and the sequence of the contributions of the ROS to the photocatalytic activity of the composite catalyst is $\cdot$O$_2^-$ > h$^+$ > $\cdot$OH.
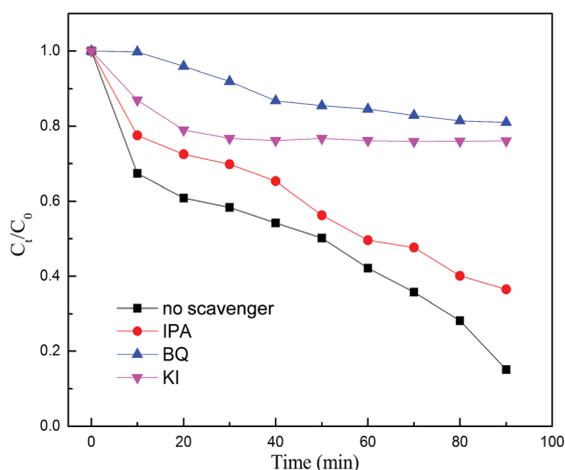
Photocatalytic mechanism. For explaining the photocatalytic degradation mechanism, the valence band edge positions of Y-La$_{0.7}$Sr$_{0.3}$MnO$_3$ and TiO$_2$ should be confirmed. The band gap energy (E_g) can be estimated from the extrapolation to the energy axis of a plot of $(Ah\nu)^2$ against $h\nu$. Fig. 11 illustrates the plots of $(Ah\nu)_2$ versus $h\nu$ for TiO$_2$ and Y-La$_{0.7}$Sr$_{0.3}$MnO$_3$ derived from the data of the UV-Vis diffuse reflectance spectra (Fig. 3),[41] using the equation:[46]

$$(Ah\nu)^n = h\nu - E_g \tag{3}$$

where E_g, A, h, and ν are the band gap, absorbance, Plank constant and light frequency, respectively. n is an index which depends on the electronic transition of the semiconductor. $n = 2$ for a direct-gap semiconductor and $n = 1/2$ for an indirect-gap one. Y-La$_{0.7}$Sr$_{0.3}$MnO$_3$ is a direct semiconductor,[47] thus, the value of n equals 2. According to Fig. 11, the band gaps energies are estimated as 1.3 and 3.2 eV for Y-La$_{0.7}$Sr$_{0.3}$MnO$_3$ and TiO$_2$, respectively.

The migration direction of the photogenerated charge carriers in the composite is related to the band edge positions of the semiconductors. The valence band (VB) and conduction band (CB) edge position of a semiconductor is estimated according to the following equation:[31]

$$E_{CB} = X - E_C - 0.5E_g \tag{4}$$

$$E_{VB} = E_{CB} + E_g \tag{5}$$

where X is the electronegativity of the semiconductor, which is defined as the geometric mean of the absolute electronegativity of the constituent atoms, E_g, E_C, E_{CB} and E_{VB} are the band gap energy, the energy of free electrons on the hydrogen scale (about 4.5 eV), and the conduction band and valence band edge potentials, respectively. The X values for Y-La$_{0.7}$Sr$_{0.3}$MnO$_3$ and TiO$_2$ were estimated to be 5.34 and 5.81 eV, respectively.

Based on the band gap structure calculations from the data of the UV-Vis diffuse reflectance spectra (Fig. 3), the calculated E_{CB} and E_{VB} edge positions of TiO$_2$ are −0.29 and 2.91 eV, respectively. As for Y-La$_{0.7}$Sr$_{0.3}$MnO$_3$, the E_{CB} and E_{VB} edge positions are 0.19 and 1.49 eV, respectively. The energy band
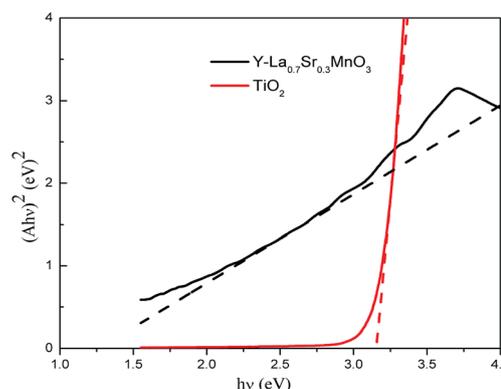

Fig. 10 Plots of photogenerated carrier trapping for the photocatalytic degradation of MO.

Fig. 11 The estimated E_g values of TiO$_2$ and Y-La$_{0.7}$Sr$_{0.3}$MnO$_3$ using UV-Vis DRS data.

structures of Y-La$_{0.7}$Sr$_{0.3}$MnO$_3$ and TiO$_2$ are schematically illustrated in Fig. 12, and it seems that the nested band structure is unfavorable for the separation of photogenerated carriers. However, it is known that Y-La$_{0.7}$Sr$_{0.3}$MnO$_3$ is a p-type semiconductor, whose Fermi energy level (E_F) is close to the valence band, and TiO$_2$ is an n-type semiconductor, whose Fermi energy level is close to the conduction band. Moreover, Fermi energy levels of semiconductors can be substantially shifted and/or pinned by surface states in a composite.[48] When the Y-La$_{0.7}$Sr$_{0.3}$MnO$_3$ semiconductor is hybridized by TiO$_2$ to form a p–n heterojunction structure, the electrons will diffuse in the opposite direction, resulting in an accumulation of negative charges in the Y-La$_{0.7}$Sr$_{0.3}$MnO$_3$ region near the junction. Also, holes diffuse from the Y-La$_{0.7}$Sr$_{0.3}$MnO$_3$ to the n-TiO$_2$ region, forming a positive section in the vicinity of the heterojunction. When the Fermi levels of Y-La$_{0.7}$Sr$_{0.3}$MnO$_3$ and TiO$_2$ align under thermodynamic equilibrium conditions, an internal electric field directed from the n-TiO$_2$ to the p-Y-La$_{0.7}$Sr$_{0.3}$MnO$_3$ is simultaneously built to stop the charge diffusion. Meanwhile, the all energy band of Y-La$_{0.7}$Sr$_{0.3}$MnO$_3$ was shifted upwards in this process whereas that of TiO$_2$ was shifted downwards until an equilibrium state of Fermi levels of p-Y-La$_{0.7}$Sr$_{0.3}$MnO$_3$ and n-TiO$_2$ was obtained after hybridization. As a result, the CB bottom of Y-La$_{0.7}$Sr$_{0.3}$MnO$_3$ became higher than that of the n-TiO$_2$ semiconductor. Under solar irradiation, Y-La$_{0.7}$Sr$_{0.3}$MnO$_3$ is excited and there is the generation of electron–hole pairs. According to the schema of Fig. 12, the photogenerated electrons move to the positive field (n-type TiO$_2$) and then react with dissolved O$_2$ in solution to produce reactive ˙O$_2^-$. At the same time, the photogenerated holes (h$^+$) move into the negative field (p-type Y-La$_{0.7}$Sr$_{0.3}$MnO$_3$) and oxidize OH$^-$ or H$_2$O to ˙OH as well as directly oxidizing MO. Thus an efficient separation of photoinduced electron–hole pairs can be achieved in the formed heterojunction between the semiconductors, which leads to better photocatalytic activity than pure Y-La$_{0.7}$Sr$_{0.3}$MnO$_3$ and pure TiO$_2$. This is in agreement with the synergetic photocatalytic effect of Y-La$_{0.7}$Sr$_{0.3}$MnO$_3$/TiO$_2$ (3.51 wt%) described above.

On the basis of the above results and previous studies, a possible enhancement mechanism for the photocatalytic activity of the Y-La$_{0.7}$Sr$_{0.3}$MnO$_3$/TiO$_2$ composite can also be proposed. Firstly, the hybridization of Y-La$_{0.7}$Sr$_{0.3}$MnO$_3$ with TiO$_2$ is beneficial to the improvement of the solar light absorbing capacity in this study, which has been demonstrated using UV-Vis DRS analysis. Secondly, the La$_{0.7}$Sr$_{0.3}$MnO$_3$/TiO$_2$ heterojunctions can enhance charge transfer and inhibit the recombination of photogenerated electron–hole pairs, which is very important for the improvement of photocatalytic activity. Hence, the Y-La$_{0.7}$Sr$_{0.3}$MnO$_3$/TiO$_2$ composite is a high-efficiency solar-light-driven magnetic photocatalyst.

Conclusions

In summary, the solar-light-driven Y-La$_{0.7}$Sr$_{0.3}$MnO$_3$/TiO$_2$ (3.51 wt%) with intrinsic magnetic properties can be synthesized and exhibits an obvious synergistic photocatalytic effect on the degradation of MO wastewater under sunlight. The enhanced photocatalytic performance could be mainly attributed to a decrease in the recombination of photogenerated carriers on the surface of the p–n heterojunction structure in Y-La$_{0.7}$Sr$_{0.3}$MnO$_3$/TiO$_2$. The photocatalytic activity of Y-La$_{0.7}$Sr$_{0.3}$MnO$_3$/TiO$_2$ (3.51 wt%) does not obviously decrease after 8 times recycling, indicating that the Y-La$_{0.7}$Sr$_{0.3}$MnO$_3$/TiO$_2$ can be recycled using an external magnetic field more easily and can be used repeatedly. It is believed that the composite Y-La$_{0.7}$Sr$_{0.3}$MnO$_3$/TiO$_2$ (3.51 wt%) photocatalyst would have potential applications in wastewater treatment in the future.

Conflicts of interest

There are no conflicts to declare.

Acknowledgements

Notes and references

1 S. P. Guo and G. C. Guo, *J. Mater. Chem. A*, 2014, **2**, 20621–20628.
2 J. Yan, S. Gao, C. Wang, *et al.*, *Mater. Lett.*, 2016, **184**, 43–46.
3 X. Qiao, Y. Huang, H. Cheng, *et al.*, *Appl. Surf. Sci.*, 2015, **359**, 259–265.
4 I. Abdulkadir, S. B. Jonnalagadda and B. S. Martincigh, *Mater. Chem. Phys.*, 2016, **178**, 196–203.
5 P. Jing, J. Li, L. Pan, *et al.*, *J. Hazard. Mater.*, 2015, **284**, 163–170.
6 T. Soltani and B. K. Lee, *J. Hazard. Mater.*, 2016, **316**, 122–133.
7 S. Kumar and A. K. Ojha, *J. Alloys Compd.*, 2015, **644**, 654–662.
8 B. Ahmed, S. Kumar, S. Kumar, *et al.*, *J. Alloys Compd.*, 2016, **679**, 324–334.
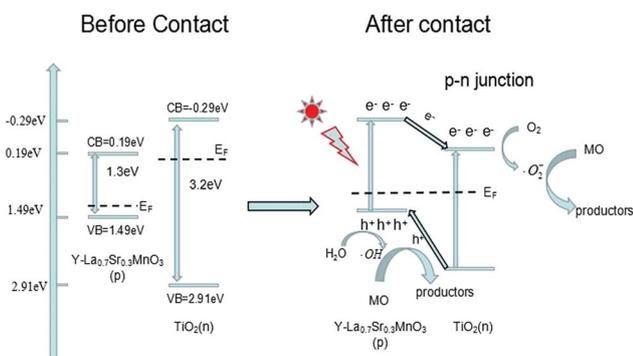9 Z. Zhu, X. Li, W. Gu, *et al.*, *J. Alloys Compd.*, 2016, **686**, 306–311.

Fig. 12 The proposed photocatalytic mechanism for the photodegradation of MO over Y-La$_{0.7}$Sr$_{0.3}$MnO$_3$/TiO$_2$.

10 S. Jabbarzare, M. Abdellahi, H. Ghayour, *et al.*, *J. Alloys Compd.*, 2016, **688**, 1125–1130.

11 Z. X. Wei, Y. Wang, J. P. Liu, C. M. Xiao and W. W. Zeng, *Mater. Chem. Phys.*, 2012, **136**, 755–761.

12 Z. X. Wei, Y. Wang, J. P. Liu, C. M. Xiao, W. W. Zeng and S. B. Ye, *J. Mater. Sci.*, 2013, **1**, 117–1126.

13 Z. X. Wei, C. M. Xiao, W. W. Zeng and J. P. Liu, *J. Mol. Catal. A: Chem.*, 2013, **370**, 35–43.

14 Z. X. Wei, S. B. Ye and X. M. Wang, *Ceram. Int.*, 2016, **42**, 9196–9203.

15 S. Daengsakul, C. Thomas, I. Thomas, *et al.*, *Nanoscale Res. Lett.*, 2009, **4**, 839–845.

16 S. Kang, B. S. Kwak, B. H. Choi, *et al.*, *J. Ind. Eng. Chem.*, 2014, **20**, 3960–3964.

17 T. Noh, J. Ryu, J. Kim, *et al.*, *J. Alloys Compd.*, 2013, **557**, 196–201.

18 Y. B. Yang, W. Yin, S. T. Wu, *et al.*, *ACS Nano*, 2015, **10**, 1240–1248.

19 J. Zhu, D. Xiao, J. Li, *et al.*, *Catal. Lett.*, 2009, **129**, 240–246.

20 M. Ghiasi and A. Malekzadeh, *Sep. Purif. Technol.*, 2014, **134**, 12–19.

21 S. N. Tijare, S. Bakardjieva, J. Subrt, *et al.*, *J. Chem. Sci.*, 2014, **126**, 517–525.

22 Y. C. Chang, C. Y. Lee and H. T. Chiu, *ACS Appl. Mater. Interfaces*, 2013, **6**, 31–35.

23 R. Abazari, S. Sanati and L. A. Saghatforoush, *Mater. Sci. Semicond. Process.*, 2014, **25**, 301–306.

24 I. Shakir, M. Sarfraz, Z. Ali, *et al.*, *J. Alloys Compd.*, 2016, **660**, 450–455.

25 Z. Han, V. W. C. Chang, L. Zhang, *et al.*, *Aerosol Air Qual. Res.*, 2012, **12**, 1327–1335.

26 Y. C. Chang, C. Y. Lee and H. T. Chiu, *ACS Appl. Mater.Interfaces*, 2013, **6**, 31–35.

27 B. Lin, Q. Li, B. Liu, *et al.*, *Nanoscale*, 2016, **8**, 8178–8188.

28 L. Yang, W. S. Guan, B. Bai, *et al.*, *J. Alloys Compd.*, 2010, **504**, L10–L13.

29 D. F. Zhang, *Russ. J. Phys. Chem. A*, 2015, **89**, 1948–1955.

30 R. Cruz-Ortiz, W. J. Jeremy, *et al.*, *J. Chem. Eng.*, 2017, **316**, 179–185.

31 H. J. Lu, L. l. Xu, B. Wei, *et al.*, *Appl. Surf. Sci.*, 2014, **303**, 360–366.

32 X. Li, H. Wang, T. Chu, *et al.*, *Mater. Res. Bull.*, 2014, **57**, 254–259.

33 K. S. Jeon, S. D. Oh, Y. D. Suh, *et al.*, *Phys. Chem. Chem. Phys.*, 2009, **11**, 534–542.

34 K. Rajkumar, P. Vairaselvi, P. Saravanan, *et al.*, *RSC Adv.*, 2015, **5**, 20424–20431.

35 R. E. Tanner, Y. Liang and E. I. Altman, *Surf. Sci.*, 2002, **506**, 251–271.

36 J. L. Ong, L. C. Lucas, G. N. Raikar and J. C. Gregory, *Appl. Surf. Sci.*, 1993, **72**, 7–13.

37 K. Kim, J. Jeong, A. K. Azad, *et al.*, *Appl. Surf. Sci.*, 2016, **365**, 38–46.

38 H. Xu, Z. Qu, S. Zhao, *et al.*, *Chem. Eng. J.*, 2016, **292**, 123–129.

39 W. Z. Si, Y. Wang, S. Zhao, *et al.*, *Environ. Sci. Technol.*, 2016, **50**, 4572–4578.

40 F. M. Wang, G. L. Li, B. X. Shen, Y. Y. Wang and C. He, *Chem. Eng. J.*, 2015, **263**, 356–363.

41 M. Ghiasi and A. Malekzadeh, *Sep. Purif. Technol.*, 2014, **134**, 12–19.

42 M. J. Sun, J. Y. Hu, C. Y. Zhai, *et al.*, *Electrochim. Acta*, 2017, **245**, 863–871.

43 J. Li, Y. C. Yin, E. Z. Liu, *et al.*, *J. Hazard. Mater.*, 2017, **321**, 183–192.

44 V. Gómez-Serrano, C. M. González-García and M. L. González-Martín, *Powder Technol.*, 2001, **116**, 103–108.

45 L. Ai, C. Zhang, L. Li, *et al.*, *Appl. Catal., B*, 2014, **148**, 191–200.

46 Y. F. Jia, C. J. Wu, B. W. Lee, *et al.*, *J. Hazard. Mater.*, 2017, **338**, 447–457.

47 R. Ren and X. K. Qin, *Rare Met. Mater. Eng.*, 2013, **42**, 140–144.

48 F. Z. Qiu, W. J. Li, F. Z. Wang, *et al.*, *Colloids Surf., A*, 2017, **517**, 25–32.